

Curved Magnetism in CrI₃Alexander Edström^{1,2}, Danila Amoroso^{3,4}, Silvia Picozzi³, Paolo Barone⁵, and Massimiliano Stengel^{1,6}¹*Institut de Ciència de Materials de Barcelona (ICMAB-CSIC), Campus UAB, 08193 Bellaterra, Spain*²*Department of Applied Physics, School of Engineering Sciences, KTH Royal Institute of Technology, AlbaNova University Center, 10691 Stockholm, Sweden*³*Consiglio Nazionale delle Ricerche CNR-SPIN, c/o Università degli Studi 'G. D'Annunzio', 66100 Chieti, Italy*⁴*NanoMat/Q-mat/CESAM, Université de Liège, B-4000 Liege, Belgium*⁵*Consiglio Nazionale delle Ricerche CNR-SPIN, Area della Ricerca di Tor Vergata, Via del Fosso del Cavaliere 100, I-00133 Rome, Italy*⁶*ICREA—Institució Catalana de Recerca i Estudis Avançats, 08010 Barcelona, Spain* (Received 28 October 2021; revised 8 March 2022; accepted 7 April 2022; published 28 April 2022)

Curved magnets attract considerable interest for their unusually rich phase diagram, often encompassing exotic (e.g., topological or chiral) spin states. Micromagnetic simulations are playing a central role in the theoretical understanding of such phenomena; their predictive power, however, rests on the availability of reliable model parameters to describe a given material or nanostructure. Here we demonstrate how noncollinear-spin polarized density-functional theory can be used to determine the flexomagnetic coupling coefficients in real systems. By focusing on monolayer CrI₃, we find a crossover as a function of curvature between a magnetization normal to the surface to a cycloidal state, which we rationalize in terms of effective anisotropy and Dzyaloshinskii-Moriya contributions to the magnetic energy. Our results reveal an unexpectedly large impact of spin-orbit interactions on the curvature-induced anisotropy, which we discuss in the context of existing phenomenological models.

DOI: 10.1103/PhysRevLett.128.177202

Introduction.—Inhomogeneous deformations in the form of local curvature are ubiquitous at the nanoscale, and currently regarded as a rich playground for new phenomena. [1–3] Understanding their effects is crucial for the materials design of tailored functionalities, e.g., in flexible electronics, as well as for the tunability of existing ones via external mechanical stimuli [4,5]. A notable example is flexoelectricity [1], i.e., the emergence of a macroscopic electric polarization in the presence of a nonuniform strain, highly attractive for piezoelectric replacements [5] or strain-enabled photovoltaics [6]. Atomically thin two-dimensional (2D) crystals and membranes, due to their extreme flexibility and natural tendency toward rippling [7], appear as the ideal class of materials to explore these effects.

Strain gradients can have a comparably strong impact on magnetism [2,3,8], via a curvature-induced modification of the spin coupling parameters, commonly referred to as *flexomagnetism* [9]. Representative examples include the emergence of curvature-induced Rashba spin-orbit coupling (SOC) [10–12], asymmetric magnon dispersions

[13], topological magnetism [14], magnetic anisotropies, and effective Dzyaloshinskii-Moriya interactions (DMI) [2,14–16]. Remarkably, the geometric DMI can drive the formation of chiral and topological spin configurations even in the absence of SOC [2], thus lifting the traditional requirement of heavy elements in the crystal structure for exotic magnetic orders to occur. An exciting development in this context is the recent experimental report of strain-gradient-induced DMI resulting in a room-temperature Skymion lattice [17]. Thanks to impressive advances in experimental fabrication and characterization techniques [18,19], additional observations of these effects in the lab are anticipated in the near future. From theory, it would be desirable to support the experimental efforts by developing a quantitatively accurate understanding of flexomagnetism in real materials. Several simplifying assumptions are currently adopted in micromagnetic simulations of curved nanostructures (see, e.g., Ref. [2] and references therein), potentially limiting their predictive power. For example, the effective DMI and anisotropy in the curved structure are modeled as nonrelativistic effects via a coordinate transformation operated on the isotropic exchange interaction. While appearing reasonable, such an approximation has not been tested in a realistic context, and its validity is still an open question.

Ab initio electronic-structure methods have played a leading role in understanding low-dimensional magnets

Published by the American Physical Society under the terms of the Creative Commons Attribution 4.0 International license. Further distribution of this work must maintain attribution to the author(s) and the published article's title, journal citation, and DOI. Funded by Bibsam.

and formulating new predictions [20–23]. Their application to flexomagnetism is, however, still at an infancy stage and technically challenging in the framework of density-functional theory (DFT): Curvature breaks translational symmetry, and its study requires, in principle, large periodic supercells that may contain several hundreds of atoms. The recent discovery of long-range magnetic order in monolayers of CrI₃ and other Van der Waals compounds [24–27] provides a natural playground to study curvature-induced effects on magnetic properties from first principles. In addition to their practical [28] and fundamental [22,29,30] interest, two-dimensional magnets with few atoms per surface unit allow for the simulation of bent geometries to be tractable (even if expensive) within DFT [31]. Nonetheless, the few existing studies have targeted collinear spin structures [31–33]. This is clearly insufficient for understanding the emergence of nontrivial magnetic states in a bent layer, which requires a fully noncollinear treatment of the spins in the presence of curvature.

Here, we use noncollinear-spin DFT to investigate the magnetic properties of CrI₃ as a function of curvature. The latter is incorporated by focusing on nanotube (NT) geometries with radii (R) between 7.5 and 30 Å. By comparing the energies of different magnetic states as functions of R , we show that curvature leads to a crossover between an out-of-plane (OP) magnetization for the flat monolayer (corresponding to a radial magnetization for large- R NTs), and a cycloidal state at larger curvatures (smaller R), which is stabilized by an effective curvature-induced DMI [16]. To rationalize this finding, we construct a continuum model, whose parameters are fully determined from first principles, in terms of the spin stiffness, anisotropy and DMI strength, and their dependence on curvature. We find that SOC, which largely originates from the I atoms in CrI₃, [34] has a surprisingly strong impact on the curvature-induced effective anisotropy, which qualitatively departs from the assumptions of earlier models.

Methods.—Calculations are performed using the projector augmented wave [35,36] method, as implemented in VASP [37–39]. The local density approximation is used for the exchange correlation together with an additional Coulomb repulsion [40] of $U = 0.5$ eV on Cr d states. The cutoff energy for the plane-waves basis set is 350 eV. [41] Calculations are performed within periodic boundary conditions, with (at least) 15 Å of vacuum separating the repeated images of the monolayers or NTs. A $4 \times 4 \times 1$ k -point mesh is used for calculations on the freestanding monolayer [42], while $4 \times 1 \times 1$ k points are used for the NTs. The NT structures are optimized considering collinear ferromagnetism until forces are smaller than 3 meV/Å. We consider (N, N) armchair NTs [43] for $N = 4, 5, 6, 7, 8, 10, 12, 16$, as illustrated in Fig. 1. This means that N units of the cell marked with a red rectangle in Fig. 1(a) are wrapped around the circumference. The Cr-Cr distance

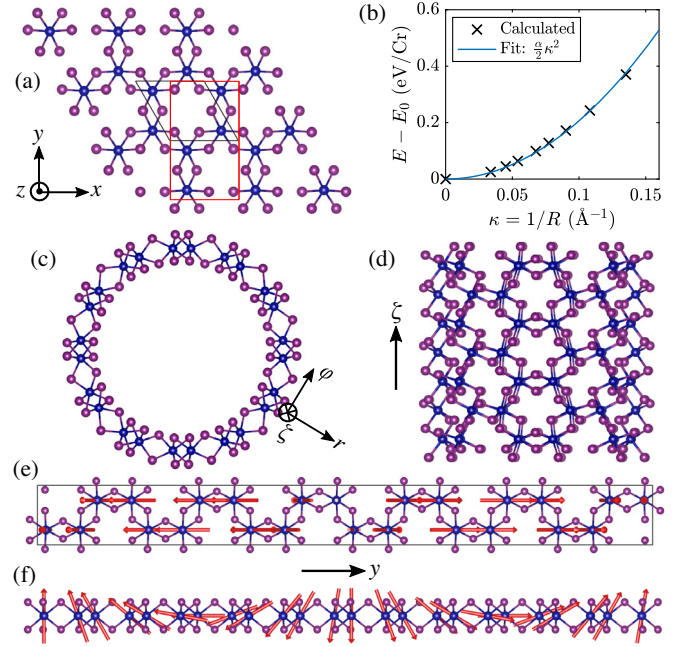


FIG. 1. (a) Monolayer CrI₃ (Cr, blue; I, purple) with black lines showing the primitive 8 atom unit cell (2 Cr and 6 I) while the red lines show the doubled unit cell, N of which are used to construct (N, N) NTs. (b) Calculated energy (per Cr) as a function of curvature. (c) $N = 6$ NT from above and (d) side. (e) Supercell strip for a spin spiral with wavelength equal to the circumference of the $N = 6$ NT, seen from above and (f) side, with arrows showing the magnetic moments $\mathbf{m}_i = [0, -\sin(qy_i), \cos(qy_i)]$.

is $d = 3.87$ Å, whereby the NT radii are approximately NR_0 with $R_0 = (3d/2\pi) = 1.85$ Å. Energy calculations on different magnetic states were performed via constrained, noncollinear magnetic calculations, with and without SOC, using a penalty energy for spins deviating from the desired configuration [44–46].

Results.—Energy differences of the relaxed NTs with collinear ferromagnetism, relative to the flat monolayer, are reported as a function of curvature $\kappa = 1/R$ in Fig. 1(b). The calculated data show a smooth monotonic behavior with κ , confirming the accuracy of the structural relaxations. The fitted bending modulus, $\alpha = 2.2$ eV, is similar to other monolayers of transition metal dichalcogenides [50]. This elastic contribution, of order 1 eV per Cr atom, dominates by far the energetics of bending. The dependence on the magnetic ordering is typically three orders of magnitude smaller (~ 1 meV/Cr), as we shall see in the following while discussing our results with noncollinear spins and SOC.

In Fig. 2, we show the energies of the three main spin states that we focus on in this Letter. They are magnetized either along the azimuthal direction $\hat{\varphi}$ (E_φ), the radial direction \hat{r} (E_r), or with all spins parallel to a direction perpendicular to $\hat{\zeta}$ (E_\perp). All energies are relative to the axial

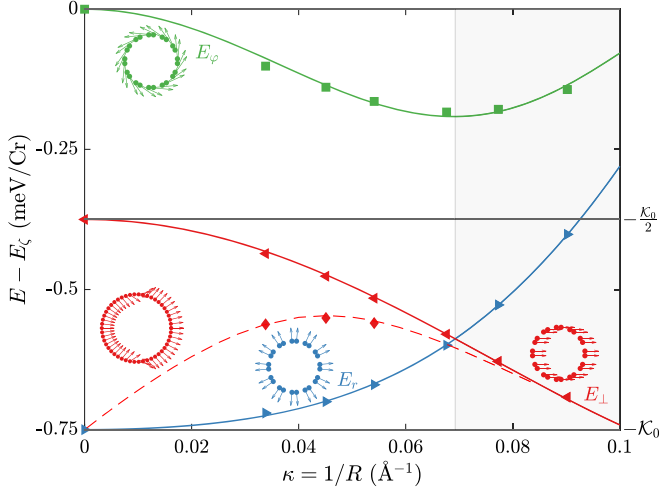


FIG. 2. Energies E_{\perp} , E_{φ} , and E_r , relative to E_{ζ} , as functions of curvature κ , for the different states schematically represented in the insets, with magnetization along $\hat{\mathbf{e}}_{\perp} \perp \hat{\zeta}$, $\hat{\varphi}$, and \hat{r} , respectively. Solid lines show energies from the continuum model discussed in the text. The dashed line shows the energy of a two-domain state [46] and red diamonds show the corresponding DFT energies.

state with spins aligned along the $\hat{\zeta}$ axis of the NT. In the large R limit we recover the known ground state of the flat monolayer, which is ferromagnetic with OP magnetization. This state is stabilized by an effective magnetic anisotropy constant $\mathcal{K}_0 = E_{\text{IP}} - E_{\text{OP}} = 0.75$ meV, defined and calculated as the energy difference between in plane (IP) and OP magnetization in the flat monolayer. [51] This corresponds to the energy difference between either azimuthal or axial (IP) magnetization and radial (OP) magnetization, in the small curvature limit. In the same limit, E_{φ} tends to zero, as the azimuthal and axial one states become degenerate, while E_r approaches $-\mathcal{K}_0$, and E_{\perp} tends to $-\mathcal{K}_0/2$ for reasons clarified shortly. At smaller R , E_{φ} decreases slightly and then increases again, overall remaining higher in energy than the other two spin states. Meanwhile, E_r increases monotonously with curvature, as the angle between neighboring spins (and hence the exchange energy) increases. Interestingly, E_{\perp} decreases, eventually leading to a crossover between the two spin configurations at $\kappa \approx 0.07 \text{ \AA}^{-1}$, where $E_r = E_{\perp}$. At larger curvatures, $E_r > E_{\perp}$, with the latter state becoming the lowest in energy among those considered here.

The possibility for curvature to profoundly affect magnetism, even leading to new chiral or topological magnetic structures, has been pointed out before [2,9]. The magnetic crossover shown in Fig. 2 is indeed reminiscent of those discussed in Ref. [16], for the opposite sign of \mathcal{K}_0 . To facilitate the discussion of our results in the context of existing continuum models, we project our magnetic configurations onto a cylindrical (locally orthogonal) coordinate system [see Fig. 1(c)], where (ζ, φ) span the tangential plane of the NT surface, and r is normal to it.

Within the (ζ, φ, r) system, the ‘‘radial’’ and ‘‘azimuthal’’ magnetization states correspond to constant values of either m_r or m_{φ} , while the ‘‘perpendicular’’ state shows a periodic out-of-phase modulation of m_r and m_{φ} along the tube circumference. More precisely, the latter state acquires the mathematical form of a spin cycloid, where $\mathbf{m}_i = [0, -\sin(qy_i), \cos(qy_i)]$ with propagation vector $q = 1/R$; an illustration is provided in Figs. 1(e)–1(f). The equal mixture of azimuthal and radial spin components in the perpendicular state explains why E_{\perp} tends to $-\mathcal{K}_0/2$ in the large-radius limit. Remarkably this also means, based on the results of Fig. 2, that curvature leads to a transition to a cycloidal magnetic ground state in the curvilinear frame of the bent surface.

In order to understand the origin of such a behavior, we consider the following continuum energy density,

$$\varepsilon = A[\partial_{\varphi} m_{\alpha}]^2 + \mathcal{K}_{\varphi} m_{\varphi}^2 + \mathcal{K}_r m_r^2 + \mathcal{D}[m_r \partial_{\varphi} m_{\varphi} - m_{\varphi} \partial_{\varphi} m_r], \quad (1)$$

where A , \mathcal{K}_{α} , and \mathcal{D} are the spin stiffness, anisotropy, and DMI parameters, $\partial_{\varphi} = (1/R)(\partial/\partial\varphi)$, and $m_{\alpha} = m_{\alpha}(\varphi)$ is one of the three curvilinear components of the magnetization density. [52] Note that all parameters in Eq. (1) depend on curvature, e.g., $A = A(\kappa = 1/R)$. To extract this dependence from our DFT calculations we fit Eq. (1), at each R , to the calculated energies of the three magnetic states in Fig. 2. The azimuthal and radial anisotropy constants are trivially provided by $\mathcal{K}_{\varphi} = E_{\varphi}$ and $\mathcal{K}_r = E_r$. Separating the remaining two parameters (A and \mathcal{D}) is computationally more involved, since their contributions to the energy of the perpendicular state, $E_{\perp} = A\kappa^2 - \mathcal{D}\kappa + \frac{1}{2}(\mathcal{K}_r + \mathcal{K}_{\varphi})$, are linearly dependent. (By symmetry, A and $\mathcal{D}\kappa$ are both even functions of κ .) To extract also $A(\kappa)$ and $\mathcal{D}(\kappa)$, we additionally perform calculations for cycloidal states of the form $\mathbf{m} = \cos(n\varphi)\hat{r} - \sin(n\varphi)\hat{\varphi}$, with integer values $n > 1$, consistent with 2π periodicity in φ . ($n = 0$ and $n = 1$ correspond to the radial and perpendicular magnetization states, already described.) This procedure allows us to uniquely resolve $A(\kappa)$, $\mathcal{D}(\kappa)$, and $\mathcal{K}(\kappa)$ at the discrete set of curvatures considered in our DFT calculations. For practical purposes, we then interpolate these data with appropriate low-order polynomials of κ (See Fig. 3 and the Supplemental Material [46]), which yields the continuous curves plotted in Fig. 2.

The resulting separate energy contributions $A\kappa^2$, $\mathcal{D}\kappa$, and \mathcal{K}_{α} from the effective spin stiffness; DMI; and anisotropy parameters are plotted as functions of curvature in Fig. 3(a). This decomposition allows us to clarify the physical origin of the cycloidal ground state obtained at larger κ . The increase in the spin stiffness energy with curvature leads to an increase in the energy cost of the spin cycloids, relative to a FM state. A nonzero \mathcal{D} (linear in κ), however, also

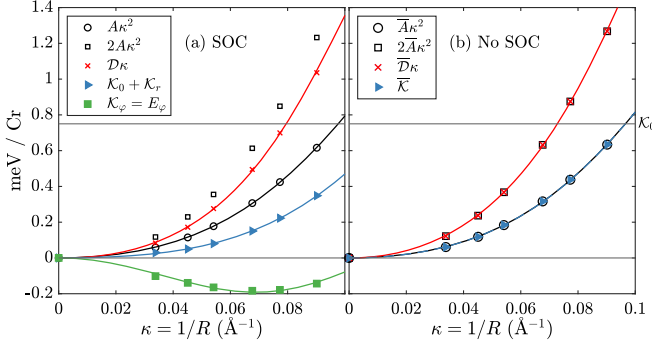


FIG. 3. Energy contributions $A\kappa^2$, $D\kappa$, and \mathcal{K} , from the effective exchange; DMI; and anisotropy terms, with SOC in (a) and without SOC in (b). Lines show fits to even, sixth order polynomials.

develops with curvature, favoring the crossover to the $n = 1$ cycloidal state. Both the curvature-induced \mathcal{D} and the flat-layer anisotropy \mathcal{K}_0 are essential to stabilizing states with $n > 0$ [46]; the latter only occurs with SOC. Note that the largest contribution to the energy comes from the DMI term, with $D\kappa \approx 1$ meV/Cr at $\kappa \approx 0.1$ Å⁻¹. Thus, the value of \mathcal{D} reaches almost 1 meV/Å, similar to the interfacial DMI of a surface of Fe on W [20,53]. For the flat, centrosymmetric CrI₃ monolayer, the DMI arises as an interaction between second neighbors, estimated to 60 μeV or even smaller [54,55], whereas electric field (\mathcal{E}) induced DMI between nearest Cr neighbors was reported to be 14 μeV for $\mathcal{E}_z \simeq 1.55$ V/nm [54]; both values are orders of magnitude smaller than the effective, curvature-induced DMI energy found here.

With the parameters of Eq. (1) at hand, we can calculate the stationary states, minimizing the continuum energy functional [46]. This confirms the transition from the radial to the “perpendicular” magnetization state at large curvatures. However, at small curvatures a qualitatively different behavior is seen; the “perpendicular” ($n = 1$ cycloid) state evolves into two domains with opposite radial magnetizations, and the energy goes to $-\mathcal{K}_0$ linearly, instead of $-\mathcal{K}_0/2$ quadratically, as shown by the red dashed line in Fig. 2. For the largest R NTs, we performed additional DFT calculations for the predicted spin configurations (red diamonds in Fig. 2), confirming the predictions of the model with excellent accuracy.

Earlier phenomenological studies [2,14–16] showed the appearance of effective anisotropy and DMI terms in curvilinear magnets, consistent with our findings. Remarkably, such effects were predicted even in the

absence of SOC. To check whether such assumptions are reliable in our case, in the following, we benchmark the model of Ref. [16], which we have adapted to our specific geometry [46], against our first-principles results. Consistent with the conclusions of Sheka *et al.* [16], we find that the coefficients of Eq. (1) are no longer independent in the absence of SOC, but enjoy the following relationships [46]:

$$\bar{\mathcal{D}} = 2\bar{A}\kappa, \quad \bar{\mathcal{K}} = \bar{\mathcal{K}}_r = \bar{\mathcal{K}}_\phi = \bar{A}\kappa^2. \quad (2)$$

(Overline symbols indicate quantities defined and calculated without SOC.) Our results of Fig. 3(a) manifestly violate such conditions: Neither the effective anisotropies nor the DMI appear to be related to the spin stiffness energy in any obvious way. To clarify the role of SOC in this unexpected behavior, we have repeated all our first-principles calculations without SOC, and followed the same postprocessing procedure to extract \bar{A} , $\bar{\mathcal{D}}$, and $\bar{\mathcal{K}}$ as functions of curvature; the energies $\bar{A}\kappa^2$, $\bar{\mathcal{D}}\kappa$, and $\bar{\mathcal{K}}$ are shown in Fig. 3(b). Without SOC, we find that Eq. (2) exactly holds within numerical accuracy. This is not unexpected as the energy no longer depends on the global quantization axis, but only on the relative angle between neighboring spins. This implies an exact degeneracy ($E_r = E_\phi = E_{n=2} = \bar{A}\kappa^2$) between the “radial,” “azimuthal,” and $n = 2$ cycloidal states on one hand, and between the “axial” and “perpendicular” states ($E_z = E_\perp = 0$) on the other. These combined facts prove that the aforementioned violation [Fig. 3(a)] of Eq. (2) is entirely due to SOC. From Eq. (1), one finds [46] that $\varepsilon_n < \varepsilon_{n-1}$ if $D > (2n - 1)A\kappa$. Specifically, $\varepsilon_{n=2} < \varepsilon_{n=1}$ if $D > 3A\kappa$. This can be compared to the above relation $\bar{\mathcal{D}} = 2\bar{A}\kappa$, whereby a SOC enhancement of \mathcal{D} by 50%, relative to A , could stabilize the $n = 2$ state, in materials with strong SOC.

The above analysis reveals an impact of relativistic effects on the curvilinear spin Hamiltonian, far more profound than previously believed. Existing models [14–16] limit their account of relativistic effects to including a curvature-independent anisotropy constant K_0 , while any impact of SOC on effective anisotropy and DMI interactions is systematically neglected. Our results show that the DMI is reduced in magnitude by around 30% by SOC, while the two anisotropy constants \mathcal{K}_ϕ and \mathcal{K}_r display a very different curvature dependence in the presence of SOC, in stark disagreement with the nonrelativistic relationships of Eq. (2). Remarkably, our calculated \mathcal{K}_ϕ is

TABLE I. Fitted leading order coefficients (energy per Cr) for the curvature dependence of spin stiffness, anisotropy, and DMI. [56].

	A_0 (meVÅ ²)	$[A_0$ (meVÅ ²)]	A_2 (eVÅ ⁴)	\mathcal{K}_0 (meV)	$\mathcal{K}_{r,2}$ (meVÅ ²)	$\mathcal{K}_{\phi,2}$ (meVÅ ²)	\mathcal{D}_1 (meVÅ ²)
No SOC	49.9	42.9	4.9	0	49.9	49.9	99.9
With SOC	48.1	40.7	4.8	0.75	17.7	-90.4	63.4

opposite in sign to what would result from the physics of isotropic exchange alone. This shows that SOC needs to be included in the calculation of the effective anisotropy of bent layers, as its neglect might lead to qualitatively wrong physical answers. For a quantitative comparison, in Table I we list the lowest-order fitted coefficients of $A(\kappa)$, $\mathcal{K}_\alpha(\kappa)$, and $\mathcal{D}(\kappa)$, with and without SOC. Clearly, the spin stiffness (A_0 and A_2) is not substantially affected by SOC. The effective DMI, $\bar{\mathcal{D}}_1 = 2\bar{A}_0 = 99.9 \text{ meV}\text{\AA}^2/\text{Cr}$ is increased compared with $\mathcal{D}_1 = 63.4 \text{ meV}\text{\AA}^2/\text{Cr}$ with SOC. The leading order change in K_φ , would correspond to $\bar{A}_0 = 49.9 \text{ meV}\text{\AA}^2/\text{Cr}$ in the view of earlier models, in clear contrast to the value of $-90.4 \text{ meV}\text{\AA}^2/\text{Cr}$ found from our DFT calculations including SOC.

Conclusions.—We have used noncollinear magnetic DFT calculations, with and without SOC, to investigate the interplay of curvature and magnetism in monolayer CrI_3 . In addition to revealing a crossover between two spin states of distinct symmetry, our calculations demonstrated that the effects of SOC are essential to consider for a quantitatively (and sometimes even qualitatively) accurate description of the flexomagnetic coupling parameters, and to stabilize the cycloidal ground state of the curved system. The obvious question is whether these conclusions are specific to the material considered here, or whether they are relevant to a broader range of systems. We can't give a definite answer at this stage, but we can certainly speculate on how effective the present strategy may be in studying other cases. The main limitation we see in this context is related to computational power: While adapting our method to other 2D layers appears straightforward, the study of thicker membranes may be out of reach at present, due to the costly NT geometry. A way forward may be provided by the so-called cyclic DFT method, [57] which allows for calculating bent structures at a significantly lower computational cost; whether such an approach is effective in noncollinear spin structures, however, remains to be seen. An alternative possibility would be treating curvature perturbatively via flexural phonons, analogous to the ongoing efforts in the theory of flexoelectricity [58]; this could possibly allow one to work with the primitive cell of the flat crystal, with considerable savings in computer power. An exploration of these promising avenues, together with the discussion of other related physical effects going beyond the Hamiltonian of Eq. (1), will be an exciting topic for future studies.

We acknowledge financial support from the Swedish Research Council (VR—2018-06807). M. S. acknowledges the support of Ministerio de Ciencia e Innovación (MICINN-Spain) through Grant No. PID2019–108573GB-C22, and Severo Ochoa FUNFUTURE center of excellence (CEX2019-000917-S); of Generalitat de Catalunya (Grant No. 2017 SGR1506); and of the European Research Council (ERC) under the European Union's Horizon

2020 research and innovation program (Grant Agreement No. 724529). P. B. and S. P. acknowledge financial support from Italian MIUR under the PRIN project “Tuning and Understanding Quantum Phases in 2D Materials—Quantum2D,” Grant No. 2017Z8TS5B and “TWEET: Towards Ferroelectricity in Two Dimensions,” Grant No. 2017YCTB59, respectively. D. A. and S. P. acknowledge financial support by the Nanoscience Foundries and Fine Analysis (NFFA-MIUR Italy) project. The authors thankfully acknowledge the computer resources at Pirineus and the technical support provided by CSUC (RES-FI-2021-1-0034). Additionally, computational work was done on resources at PDC, Stockholm, via the Swedish National Infrastructure for Computing (SNIC).

-
- [1] P. Zubko, G. Catalan, and A. K. Tagantsev, *Annu. Rev. Mater. Res.* **43**, 387 (2013).
 - [2] R. Streubel, P. Fischer, F. Kronast, V. P. Kravchuk, D. D. Sheka, Y. Gaididei, O. G. Schmidt, and D. Makarov, *J. Phys. D* **49**, 363001 (2016).
 - [3] D. D. Sheka, *Appl. Phys. Lett.* **118**, 230502 (2021).
 - [4] H. Lu, C.-W. Bark, D. Esque de los Ojos, J. Alcalá, C. B. Eom, G. Catalan, and A. Gruverman, *Science* **336**, 59 (2012).
 - [5] U. K. Bhaskar, N. Banerjee, A. Abdollahi, Z. Wang, D. G. Schlom, G. Rijnders, and G. Catalan, *Nat. Nanotechnol.* **11**, 263 (2016).
 - [6] L. Shu, S. Ke, L. Fei, W. Huang, Z. Wang, J. Gong, X. Jiang, L. Wang, F. Li, S. Lei, Z. Rao, Y. Zhou, R.-K. Zheng, X. Yao, Y. Wang, M. Stengel, and G. Catalan, *Nat. Mater.* **19**, 605 (2020).
 - [7] A. Fasolino, J. H. Los, and M. I. Katsnelson, *Nat. Mater.* **6**, 858 (2007).
 - [8] O. M. Volkov, A. Kákay, F. Kronast, I. Mönch, M.-A. Mawass, J. Fassbender, and D. Makarov, *Phys. Rev. Lett.* **123**, 077201 (2019).
 - [9] R. Hertel, *SPIN* **03**, 1340009 (2013).
 - [10] P. Gentile, M. Cuoco, and C. Ortix, *SPIN* **03**, 1340002 (2013).
 - [11] P. Gentile, M. Cuoco, and C. Ortix, *Phys. Rev. Lett.* **115**, 256801 (2015).
 - [12] A. Pyatakov, A. Sergeev, F. Mikailzade, and A. Zvezdin, *J. Magn. Magn. Mater.* **383**, 255 (2015), selected papers from the sixth Moscow International Symposium on Magnetism (MISM-2014).
 - [13] J. A. Otálora, M. Yan, H. Schultheiss, R. Hertel, and A. Kákay, *Phys. Rev. Lett.* **117**, 227203 (2016).
 - [14] O. V. Pylypovskiy, V. P. Kravchuk, D. D. Sheka, D. Makarov, O. G. Schmidt, and Y. Gaididei, *Phys. Rev. Lett.* **114**, 197204 (2015).
 - [15] Y. Gaididei, V. P. Kravchuk, and D. D. Sheka, *Phys. Rev. Lett.* **112**, 257203 (2014).
 - [16] D. D. Sheka, V. P. Kravchuk, and Y. Gaididei, *J. Phys. A* **48**, 125202 (2015).
 - [17] Y. Zhang, J. Liu, Y. Dong, S. Wu, J. Zhang, J. Wang, J. Lu, A. Rückriegel, H. Wang, R. Duine, H. Yu, Z. Luo, K. Shen, and J. Zhang, *Phys. Rev. Lett.* **127**, 117204 (2021).

- [18] A. Fernández-Pacheco, R. Streubel, O. Fruchart, R. Hertel, P. Fischer, and R. P. Cowburn, *Nat. Commun.* **8**, 15756 (2017).
- [19] C. Donnelly, M. Guizar-Sicairos, V. Scagnoli, S. Gliga, M. Holler, J. Raabe, and L. J. Heyderman, *Nature (London)* **547**, 328 (2017).
- [20] M. Heide, G. Bihlmayer, and S. Blügel, *Physica (Amsterdam)* **404B**, 2678 (2009).
- [21] C. Xu, J. Feng, H. Xiang, and L. Bellaiche, *npj Comput. Mater.* **4**, 57 (2018).
- [22] D. Amoroso, P. Barone, and S. Picozzi, *Nat. Commun.* **11**, 5784 (2020).
- [23] S. Tiwari, M. L. Van de Put, B. Sorée, and W. G. Vandenberghe, *npj 2D Mater. Appl.* **5**, 54 (2021).
- [24] B. Huang, G. Clark, E. Navarro-Moratalla, D. R. Klein, R. Cheng, K. L. Seyler, D. Zhong, E. Schmidgall, M. A. McGuire, D. H. Cobden, W. Yao, D. Xiao, P. Jarillo-Herrero, and X. Xu, *Nature (London)* **546**, 270 (2017).
- [25] C. Gong, L. Li, Z. Li, H. Ji, A. Stern, Y. Xia, T. Cao, W. Bao, C. Wang, Y. Wang, Z. Q. Qiu, R. J. Cava, S. G. Louie, J. Xia, and X. Zhang, *Nature (London)* **546**, 265 (2017).
- [26] M. A. McGuire, *Crystals* **7**, 121 (2017).
- [27] K. S. Burch, D. Mandrus, and J.-G. Park, *Nature (London)* **563**, 47 (2018).
- [28] T. Song, X. Cai, M. W.-Y. Tu, X. Zhang, B. Huang, N. P. Wilson, K. L. Seyler, L. Zhu, T. Taniguchi, K. Watanabe, M. A. McGuire, D. H. Cobden, D. Xiao, W. Yao, and X. Xu, *Science* **360**, 1214 (2018).
- [29] M.-G. Han, J. A. Garlow, Y. Liu, H. Zhang, J. Li, D. DiMarzio, M. W. Knight, C. Petrovic, D. Jariwala, and Y. Zhu, *Nano Lett.* **19**, 7859 (2019).
- [30] X. Yao, Y. Wang, and S. Dong, *Int. J. Mod. Phys. B* **35**, 2130004 (2021).
- [31] A. V. Kuklin, M. A. Visotin, W. Baek, and P. V. Avramov, *Physica (Amsterdam)* **123E**, 114205 (2020).
- [32] Y.-H. Shen, Y.-X. Song, W.-Y. Tong, X.-W. Shen, S.-j. Gong, and C.-G. Duan, *Adv. Theor. Simul.* **1**, 1800048 (2018).
- [33] W. Shi, Y. Guo, Z. Zhang, and W. Guo, *J. Phys. Chem. C* **123**, 24988 (2019).
- [34] J. L. Lado and J. Fernández-Rossier, *2D Mater.* **4**, 035002 (2017).
- [35] P. E. Blöchl, *Phys. Rev. B* **50**, 17953 (1994).
- [36] G. Kresse and D. Joubert, *Phys. Rev. B* **59**, 1758 (1999).
- [37] G. Kresse and J. Furthmüller, *Comput. Mater. Sci.* **6**, 15 (1996).
- [38] G. Kresse and J. Hafner, *Phys. Rev. B* **49**, 14251 (1994).
- [39] G. Kresse and J. Hafner, *Phys. Rev. B* **47**, 558 (1993).
- [40] S. L. Dudarev, G. A. Botton, S. Y. Savrasov, C. J. Humphreys, and A. P. Sutton, *Phys. Rev. B* **57**, 1505 (1998).
- [41] The value of U and other computational settings are chosen in accordance with Ref. [21].
- [42] Using $8 \times 8 \times 1$ k -points changes the magnetic anisotropy of the monolayer by less than 3%.
- [43] M. Dresselhaus, G. Dresselhaus, and R. Saito, *Carbon* **33**, 883 (1995).
- [44] D. Hobbs, G. Kresse, and J. Hafner, *Phys. Rev. B* **62**, 11556 (2000).
- [45] P.-W. Ma and S. L. Dudarev, *Phys. Rev. B* **91**, 054420 (2015).
- [46] See Supplemental Material at <http://link.aps.org/supplemental/10.1103/PhysRevLett.128.177202> for a detailed discussion about the fitting procedure for $A(1/R)$ and $\mathcal{D}(1/R)$, calculations without constraints on the spin directions and confirmations that the energy differences studied are independent of the constraint value, comparison to other continuum models, and discussion of stationary states of the continuum energy and related magnetic domain walls. Additionally contains Refs. [47–49].
- [47] O. Besbes, S. Nikolaev, N. Meskini, and I. Solovyev, *Phys. Rev. B* **99**, 104432 (2019).
- [48] I. V. Kashin, V. V. Mazurenko, M. I. Katsnelson, and A. N. Rudenko, *2D Mater.* **7**, 025036 (2020).
- [49] S. Grytsiuk, M. Hoffmann, J.-P. Hanke, P. Mavropoulos, Y. Mokrousov, G. Bihlmayer, and S. Blügel, *Phys. Rev. B* **100**, 214406 (2019).
- [50] S. Kumar and P. Suryanarayana, *Nanotechnology* **31**, 43LT01 (2020).
- [51] Note that \mathcal{K}_0 , in addition to the single-ion anisotropy, also accounts for anisotropic symmetric exchange, whose importance in CrI_3 was recently pointed out. [21].
- [52] We consider m_α as a constant function of the axial ζ coordinate.
- [53] Considering an area of $19.5 \text{ \AA}^2/\text{Cr}$.
- [54] S. I. Vishkayi, Z. Torbatian, A. Qaiumzadeh, and R. Asgari, *Phys. Rev. Mater.* **4**, 094004 (2020).
- [55] Y. O. Kvashnin, A. Bergman, A. I. Lichtenstein, and M. I. Katsnelson, *Phys. Rev. B* **102**, 115162 (2020).
- [56] The value of A_0 in brackets was obtained from spin cycloid energies of the flat monolayer, showing a moderate numerical discrepancy to the value fitted including the curved systems.
- [57] A. S. Banerjee and P. Suryanarayana, *J. Mech. Phys. Solids* **96**, 605 (2016).
- [58] M. Stengel and D. Vanderbilt, First-principles theory of flexoelectricity, in *Flexoelectricity in Solids* (World Scientific Publishing Co., Singapore, 2016), Chap. Chapter 2, pp. 31–110.